Label-free live brain imaging and targeted patching with third-harmonic generation microscopy

Stefan Witte[a,b,1], Adrian Negrean[a,b,c], Johannes C. Lodder[b,c], Christiaan P. J. de Kock[b,c], Guilherme Testa Silva[b,c], Huibert D. Mansvelder[b,c,2], and Marie Louise Groot[a,b,2]

[a]Biophysics Group, Institute for Lasers, Life, and Biophotonics Amsterdam, VU University, De Boelelaan 1081, 1081 HV, Amsterdam, The Netherlands; [c]Integrative Neurophysiology, Centre for Neurogenomics and Cognitive Research, VU University, De Boelelaan 1085, 1081 HV, Amsterdam, The Netherlands; and [b]Neuroscience Campus Amsterdam, De Boelelaan 1085, 1081 HV, Amsterdam, The Netherlands

Edited* by Margaret M. Murnane, University of Colorado, Boulder, CO, and approved February 18, 2011 (received for review December 15, 2010)

The ability to visualize neurons inside living brain tissue is a fundamental requirement in neuroscience and neurosurgery. Especially the development of a noninvasive probe of brain morphology with micrometer-scale resolution is highly desirable, as it would provide a noninvasive approach to optical biopsies in diagnostic medicine. Two-photon laser-scanning microscopy (2PLSM) is a powerful tool in this regard, and has become the standard for minimally invasive high-resolution imaging of living biological samples. However, while 2PLSM-based optical methods provide sufficient resolution, they have been hampered by the requirement for fluorescent dyes to provide image contrast. Here we demonstrate high-contrast imaging of live brain tissue at cellular resolution, without the need for fluorescent probes, using optical third-harmonic generation (THG). We exploit the specific geometry and lipid content of brain tissue at the cellular level to achieve partial phase matching of THG, providing an alternative contrast mechanism to fluorescence. We find that THG brain imaging allows rapid, noninvasive label-free imaging of neurons, white-matter structures, and blood vessels simultaneously. Furthermore, we exploit THG-based imaging to guide micropipettes towards designated neurons inside live tissue. This work is a major step towards label-free microscopic live brain imaging, and opens up possibilities for the development of laser-guided microsurgery techniques in the living brain.

biomedical imaging | biophotonics | neuro-imaging | nonlinear optics

High-resolution imaging is an essential technique in many areas of science. In diagnostic medicine, the ability to perform a noninvasive optical biopsy (1, 2) of various types of tissue with micrometer-scale resolution would provide a major step forward. While two-photon laser-scanning microscopy (2PLSM)-based methods have revolutionized biological imaging (3, 4), they require fluorescent probes to provide image contrast. Such probes may interfere with cellular function and are usually not practical for biomedical applications. Other nonlinear interaction mechanisms can provide intrinsic, label-free image contrast in nonlinear microscopy, such as second-harmonic generation (SHG) (5), third-harmonic generation (THG) (6–10), coherent anti-Stokes Raman scattering (11, 12), and stimulated Raman scattering (13).

Here we show that specifically THG microscopy is a powerful and versatile tool for label-free live brain imaging. THG is a well known nonlinear optical phenomenon (14), which has the interesting property that the phase-matching conditions required for efficient THG can be enhanced by the presence of discontinuities within the focal volume of a laser beam. In imaging, THG microscopy has been shown to provide contrast in transparent samples (15), and its potential has been explored for dermatological studies (16, 17), zebrafish embryogenesis (18), and zebrafish nervous system imaging (19). While these studies demonstrate the excellent possibilities of label-free microscopy, THG imaging provided only partial information, and had to be augmented by SHG and/or two-photon-excited auto-fluorescence imaging. In stark contrast, we find that the composition of the living brain is very well suited for THG imaging, providing excellent structural contrast using only a single imaging modality, without the need for externally applied contrast agents.

Results and Discussion

Third-Harmonic Generation Microscopy. The principle of THG brain imaging is shown in Fig. 1*A*. Our setup consists of a 2PLSM microscope with a femtosecond optical parametric oscillator (OPO) as the light source (see *Materials and Methods* and Fig. S1). The OPO generates 200 fs pulses with a repetition frequency of 80 MHz, tunable between 1,050 and 1,500 nm. The maximum available output energy after the microscope objective is ~200 mW. The laser wavelength needed for THG is longer than typically used in 2PLSM, as the produced THG signal will be at exactly one third of the excitation wavelength. For THG imaging, wavelengths in the range of 1,200–1,350 nm provide optimum contrast. While the use of shorter wavelength still provides significant contrast, the THG signal is then produced at UV wavelengths that are more readily absorbed by the tissue and less efficiently collected by the microscope optics. Wavelengths above 1,350 nm suffer from excessive water absorption, which prevents deep-tissue imaging. An added advantage of using longer wavelengths is the increased depth penetration and reduced photodamage compared to the Ti:Sapphire wavelength range (20).

The efficiency of THG depends mainly on the third-order susceptibility $\chi^{(3)}$ of the medium and the phase-matching conditions. The total generated THG intensity by a laser beam with intensity I_ω and angular frequency ω in a medium is given by (14):

$$I_{\mathrm{THG}} = \left(\frac{3\omega}{2n_\omega c}\right)^2 \chi^{(3)} I_\omega^3 \int_{z1}^{z2} \frac{e^{i\Delta kz}}{(1+2iz/b)^2} dz, \qquad [1]$$

where n_ω is the refractive index of the medium for the incident beam, c is the speed of light, $\Delta k = (n_{3\omega}3\omega/c)\text{-}3(n_\omega\omega/c)$ is the phase mismatch, z is the position along the beam axis, z_1 and z_2 are the boundaries of the medium, and b is the confocal parameter of the focused laser beam.

In a homogeneous medium with a positive phase mismatch Δk, the phase-matching integral in Eq. **1** goes to zero and no THG is produced, irrespective of the magnitude of I_ω and $\chi^{(3)}$. Note that practically all materials have a positive phase mismatch in the visible wavelength range. In contrast, partial phase

Author contributions: S.W., A.N., H.D.M., and M.L.G. designed research; S.W., A.N., J.C.L., C.P.J.d.K., and G.T.S. performed research; S.W. analyzed data; and S.W., H.D.M., and M.L.G. wrote the paper.

The authors declare no conflict of interest.

*This Direct Submission article had a prearranged editor.

[1]To whom correspondence should be addressed. E-mail: s.m.witte@vu.nl.

[2]H.D.M. and M.L.G. share senior authorship.

This article contains supporting information online at www.pnas.org/lookup/suppl/doi:10.1073/pnas.1018743108/-/DCSupplemental.

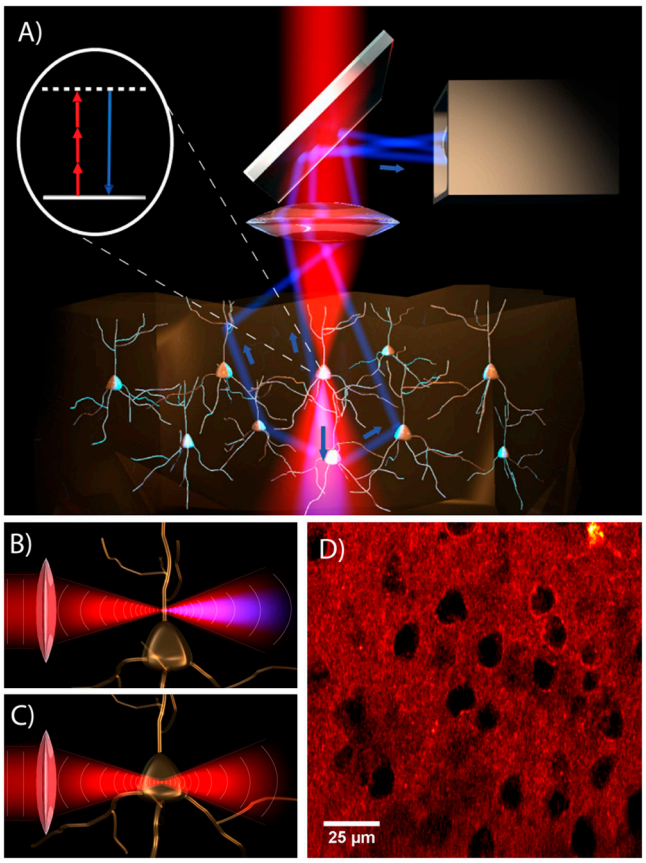

Fig. 1. Label-free live brain imaging using third-harmonic generation microscopy. (*A*) Schematic of THG microscopy on brain tissue in an epidetection geometry. Inset: Principle of THG. Note that no optical excitation of the medium takes place. (*B*) Focused laser beam at a dendrite. By setting the laser focal volume several times larger than the dendrite diameter, partial phase matching is achieved, and a significant THG signal is produced. (*C*) Focused laser beam in the cell body. Due to the poor structural phase-matching conditions, no THG is produced. (*D*) THG microscopy image of living neurons in mouse brain tissue. The somata appear as dark shadows.

matching can be achieved by introducing a small inhomogeneity at the focus, resulting in a finite THG signal. Detailed calculations show that the maximum value of the integral in Eq. **1** is reached when a structure is half the size of the focal volume (21).

THG Imaging of Live Brain Tissue. As a result of these underlying physical principles, the phase-matching conditions for THG are governed by the specific structure and composition of the material within the laser focus, and can be controlled through the focusing parameters of the laser. Brain tissue consists for a large part of axons and dendrites, with typical diameters in the range of 0.3–2 μm (22, 23). These structures contain a high concentration of lipids, which are known to have a high $\chi^{(3)}$ (9). By setting the focal volume of the incident laser beam to several times the size of a typical dendrite, we create a geometry where the phase-matching conditions enable efficient THG (21) (Fig. 1*B*). In contrast, neuronal cell bodies mostly contain organelles that are much smaller, mainly having structures at the 20–100 nm length scale. These smaller structures do not produce a significant THG signal for our 3 μm focal length. As a result, THG is suppressed inside the neurons (Fig. 1*C*). By setting the focusing conditions in this way we create a "shadow contrast" image, enabling high-resolution visualization of neurons inside live brain tissue in a noninvasive way, without the need for fluorescent dyes or genetic probes. A typical THG image of neurons in the neocortex of a mouse is displayed in Fig. 1*D*, showing this shadow contrast with clearly distinguishable cell bodies.

An initial study on THG signals from neuronal membranes was reported by Yelin et al. (8), who used isolated cultured neurons on a coverslip. It should be stressed that due to the highly different geometrical phase-matching conditions in live bulk tissue compared to isolated cells, the conditions for THG are very different in the present case.

For THG imaging, we typically use several tens of mW close to the sample surface, and increase the energy up to 200 mW at higher depths to compensate for intensity losses due to light scattering and focusing aberrations introduced by the tissue. While these average laser powers may seem high compared to typical values used in 2PLSM, the long wavelength and the absence of resonant excitation ensure that tissue viability is maintained even after extensive imaging. As THG does not lead to photobleaching, phototoxicity is also minimized compared to fluorescence excitation. We have continuously recorded images at a fixed location for >30 minutes without significant changes in signal strength or tissue morphology.

For a practical optical biopsy, backward (epi-)detection is a fundamental requirement. Although THG is only produced in the forward direction, at 400 nm the scattering length is several times shorter than the absorption length. This tissue property ensures that a significant fraction of the generated THG photons is scattered back towards the sample surface (24), enabling efficient epidetection as depicted schematically in Fig. 1*A*.

To characterize the response of the tissue to light at a wavelength of 1,200 nm, we use a broadband emission filter (380–700 nm) to collect the fluorescence and harmonic signals over this large bandwidth. A direct comparison between images taken with this broadband filter and images recorded with a narrowband filter at the THG wavelength shows that the epicollected signal is dominated by the THG signal, which comprises >85% of the detected photons. These observations confirm that molecular excitation and photobleaching do not influence THG image formation in brain tissue.

To investigate the lipid origin of the $\chi^{(3)}$, brain tissue was stained with Nile Red, a hydrophobic fluorescent probe which only exhibits fluorescence in lipid environments (25). Comparing simultaneously measured THG and 2PLSM fluorescence images shows excellent correlation outside the cell bodies (Fig. 2 *A* and *B*). Inside the neurons, the lipid-rich endoplasmic reticulum (ER) is brightly stained by the Nile Red, while this structure remains much fainter in the THG images because the ER mostly contains structures at the 20–100 nm scale, which do not provide significant THG contrast. To exclude the possibility that the Nile Red influences the THG signal in any way, we acquired THG images before and after Nile Red staining and found them to be identical. These observations confirm that a significant THG signal is only obtained in the presence of both the high $\chi^{(3)}$ from the lipids and the structural phase matching from the brain tissue geometry.

Label-Free Imaging of Various Brain Structures. The ability to image tissue structure and organization is demonstrated in Fig. 2 *C–F*. A THG scan of the dentate gyrus brain region in an unstained acute rat brain slice is shown in Fig. 2*C*. The sensitivity to lipids can be exploited effectively in the visualization of white-matter structures due to their lipid-rich myelin sheaths. Fig. 2*D* displays a THG image of the white-matter structure Corpus Callosum in a mouse brain slice, clearly showing axon bundles. The 3D-imaging capability is demonstrated in Movie S1, showing a 3D-projection of a volume scan through the Corpus Callosum. In comparison to other white-matter imaging techniques (13, 26, 27), THG imaging has the significant advantage of imaging gray matter structures simultaneously, using only a single laser beam and detector, and at near-real-time speed. Fig. 2*E* shows a THG image of the

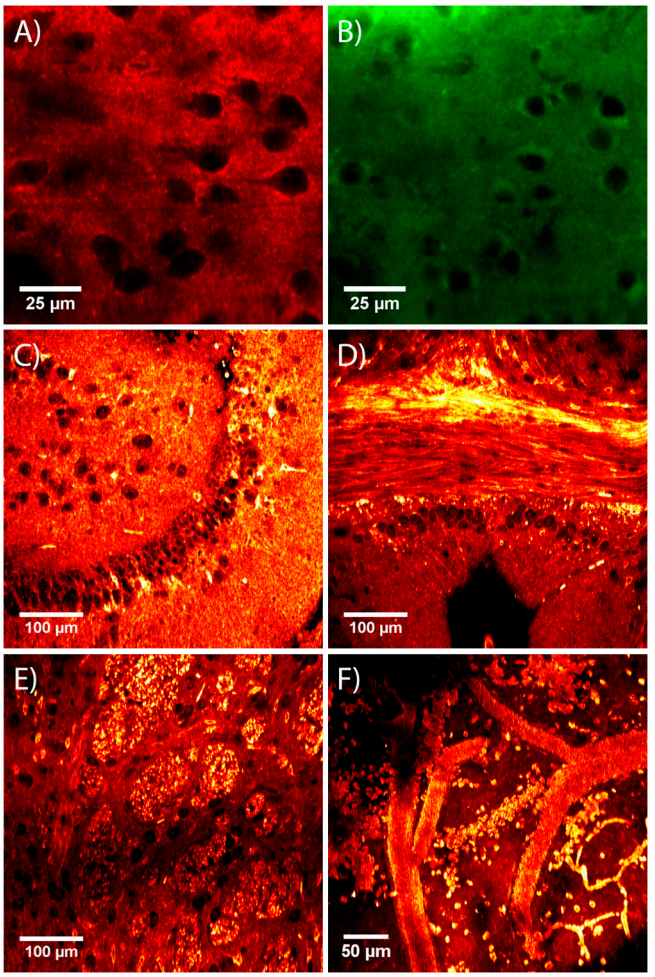

Fig. 2. THG microscopy image of living brain tissue. (*A*) THG image of mouse neocortex. (*B*) 2-photon fluorescence from Nile Red-stained lipid structures at the same location as *A*. (*C*) THG image of rat dentate gyrus (horizontal section). (*D*) THG image of mouse Corpus Callosum, axon fiber bundles are clearly resolved. A 3D-projection of this structure is shown in Movie S1. (*E*) THG image of striatum in a mouse brain (coronal section). Both white-matter fibers and neurons are clearly visible. The bright grainy structures are axon bundles that run perpendicular to the image plane. A 3D-projection at this location is shown in Movie S2. (*F*) THG image of blood vessels in the top layer of the cerebral cortex of a live, anesthetized mouse (average intensity projection of a 50 μm *z*-stack).

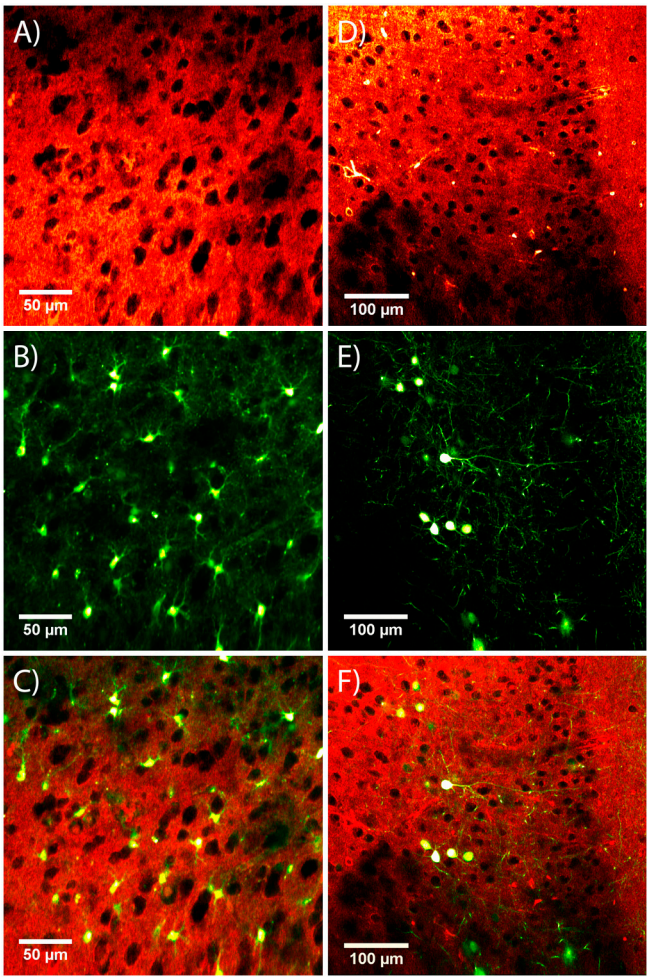

Fig. 3. Combined THG and 2PLSM imaging. (*A*) THG image of mouse prefrontal cortex. (*B*) 2PLSM image of astrocytes labeled with SR-101. (*C*) Overlay of *A* and *B*, providing information on the distribution of astrocytes within the neuronal network. (*D*) THG image of mouse prefrontal cortex. (*E*) 2-photon fluorescence image of GFP-labeled somatostatin-positive neurons. (*F*) Image overlay of *D* and *E*, showing the distribution of somatostatin-positive cells in the structure of the PFC.

striatum in a mouse brain slice, where both neurons and axon bundles are clearly resolved. Note that the axon bundles run perpendicular to the image plane, so that a cross-section of the bundles is seen. The axon bundles can be visualized more clearly by performing a depth scan at this location, of which a 3D-projection is shown in Movie S2.

Simultaneous SHG imaging can be performed by adding a second photomultiplier. Due to the absence of collagen in brain extracellular matrix and its amorphous structure, phase matching of SHG in gray matter structures is not feasible (Fig. S2, *SI Text*). Nevertheless, SHG imaging can be used to visualize axon bundles, because uniform polarity microtubule arrays inside axons provide the required phase-matching conditions for SHG (26).

In addition to neuronal imaging, THG microscopy enables imaging of vasculature (28) simultaneously without external contrast agents (Fig. 2*F*, Fig. S3). The hemoglobin in red blood cells is known to be a major source of THG signal when using 1,200–1,300 nm excitation light (15), through near-resonant excitation of the Soret band of the heme cofactor, which has a high nonlinear excitation cross-section due to its porphyrin structure (29).

Combined THG and Fluorescence Imaging. Further information on the structures that are observed with THG imaging is obtained by using specific fluorescent markers for identification (30), as illustrated in Fig. 3. Details about the imaging procedures are listed in the *Materials and Methods* section. We employ the dye Sulforhodamine-101 (SR-101) to label astrocytes (31) in an acute slice of mouse prefrontal cortex. Incidentally, two-photon excitation of SR-101 at 1,200 nm is very efficient, allowing simultaneous acquisition of THG and SR-101 fluorescence images. Typical THG and 2PLSM images are shown in Fig. 3 *A* and *B*, respectively, while the overlay is displayed in Fig. 3*C*. This data provides evidence that astrocyte cell bodies are slightly visible in the THG images, albeit at significantly lower contrast due to their smaller size.

Genetic fluorescent markers such as Green Fluorescent Protein (GFP) are useful in identifying specific neuronal cell types. As an example, we have performed imaging experiments on transgenic mouse brain expressing GFP in somatostatin-positive interneurons (32). Combined THG imaging and GFP-2PLSM provides information on the distribution of these specific

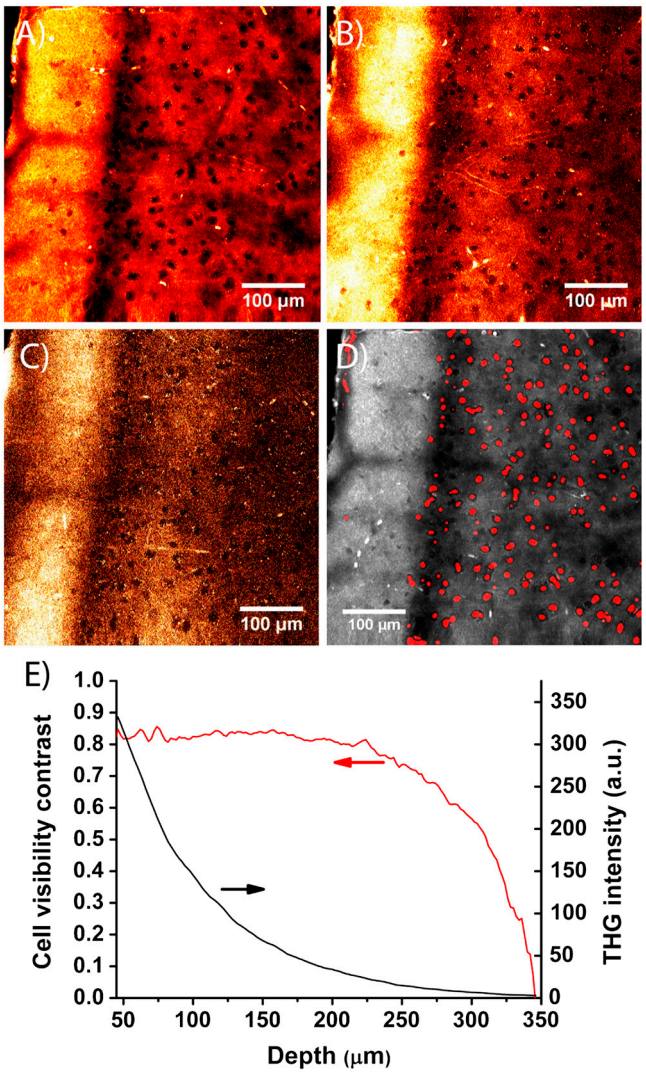

Fig. 4. THG Imaging depth and automated cell detection. (*A–C*) THG images of mouse prefrontal cortex, taken at depths of 100, 200, and 300 μm, respectively. Each image is a maximum intensity projection of three separate images spaced by 2 micron in depth. (*D*) Automatic cell detection of neurons in a THG image at 110 μm depth. The pixels that the cell detection algorithm identifies as being inside a neuron are indicated in red. (*E*) Red trace: cell visibility contrast of the image stack from which (*A–C*) are taken. Black trace: the average detected THG intensity as a function of depth.

interneurons in e.g., the neocortex and hippocampus. Separate THG and GFP recordings in the prefrontal cortex are shown in Fig. 3 *D* and *E*, respectively. The overlay in Fig. 3*F* then clearly identifies the specific interneurons within the larger network of cells.

Deep-Tissue Imaging and Automated Cell Detection. We studied the achievable depth range for THG brain imaging using acute brain slices of mouse prefrontal cortex (PFC). Epidetected THG images at increasing depth are shown in Fig. 4 *A–C*. The neurons remain visible at depths >300 μm. A depth scan through a 350 μm thick coronal section of PFC is shown in Movie S3.

To quantify cell visibility as a function of depth, a data analysis routine is written to automatically detect neuronal cell bodies (see *SI Text* for details). We define the cell visibility contrast as $(I_{\text{outside}}\text{-}I_{\text{cell}})/I_{\text{outside}}$, where I_{outside} and I_{cell} are the average THG signal inside and outside the cell, respectively. Interestingly, the contrast retains a nearly constant high value of 0.8 over a depth range of ~250 μm, although the THG signal decreases by an order of magnitude (Fig. 4*E*). This observation shows that THG brain imaging robustly detects neurons over a large depth range. The thickness of the sample (350 μm) may well be a limiting factor in these measurements, as it limits the amount of backscattered THG photons at high depths. These measurements also indicate that increasing the laser intensity can provide a further improvement in achievable depth range, which is enhanced by the THG signal's I^3-dependence. Using the automated cell detection, the location and approximate shape of the cell bodies can be reconstructed for all neurons in the imaged tissue volume, as shown in Fig. 4*D*, Movie S4. Such rapid automated cell counting can be a useful diagnostic tool for investigating tissue health in both pathology and live-tissue screening.

Label-Free Targeted Patching of Live Neurons. The geometric signal origin and high depth penetration make THG imaging ideally suited for laser-guided microsurgery applications. Small electrodes and glass pipettes are readily visualized, due to the significantly different refractive index and $\chi^{(3)}$ of glass with respect to water and tissue, providing a large discontinuity at the focus and therefore a high THG signal. We investigate this feature

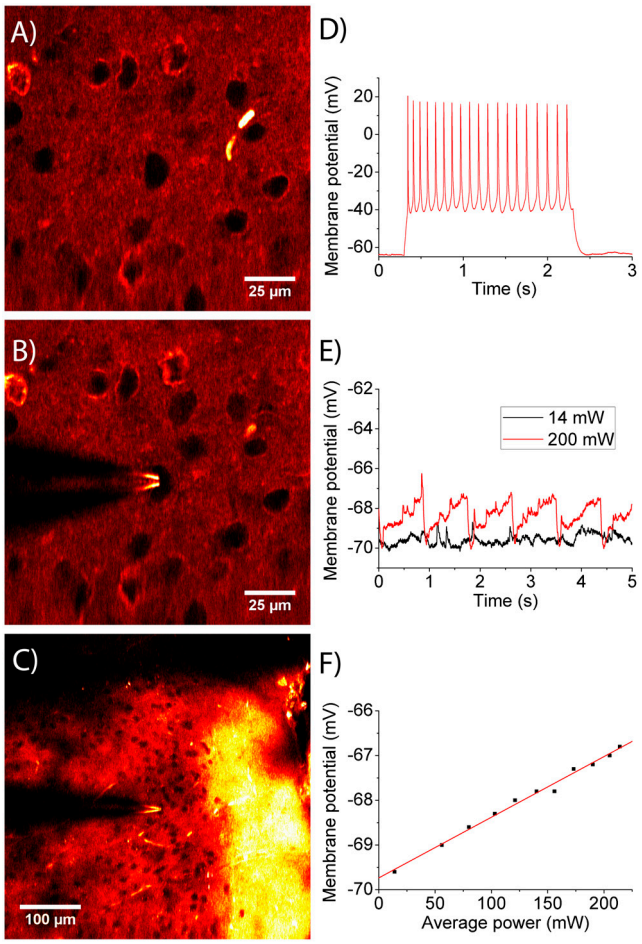

Fig. 5. Label-free targeted patching and cell viability. (*A*) THG image of mouse neocortex. (*B*) THG image at the same location after THG-guided patch-clamping of a neuron. (*C*) Large field-of-view THG image of a patched neuron at a depth of 200 μm (average of five images spaced by 2 μm in depth). (*D*) Recording of a train of action potentials from the patched neuron shown in *B* upon stimulation with a 100 pA current pulse. (*E*) Measured change in resting membrane potential during THG scanning. Even at maximum power, only a 4% voltage change is observed, which remains fully reversible. The 0.8 s periodicity corresponds to the image scanning time. (*F*) Maximum observed change in resting membrane potential vs. laser power during scanning. No nonlinear effects are present.

by performing label-free targeted patch-clamp recording, guided by THG microscopy. This experiment demonstrates the capability to perform targeted patching in an epidetection geometry without the use of fluorescent dyes. With this approach, we have successfully performed targeted patching at >200 micrometer depths in unstained brain slices, using only epidetection. Significant advantages of our THG-guided patching technique over two-photon targeted patching (33, 34) using dye-filled pipettes are the ability to choose the target neuron before entering the tissue, the larger field-of-view, and the fact that potentially harmful dyes are not required. The main advantage, however, is the fact that THG-guiding is not limited to patch pipettes, but can be extended to electrodes or even small surgical tools, which opens up significant possibilities for laser-guided microsurgery applications.

The achieved imaging speed is sufficient for live-cell patching. Movie S5 displays a typical patching experiment at real-time speed. Fig. 5*A* shows a cortical neuron before patching, while Fig. 5*B* shows the same neuron after successful patch-clamping. A large field-of-view image of a patched cell at a depth of 200 μm is presented in Fig. 5*C*. Fig. 5*D* displays an action potential recording from the patched neuron shown in Fig. 5*B* in response to an injected current pulse.

A crucial issue for many applications is whether the high laser intensity influences the neurons in any way. The targeted patching discussed above enables us to directly address this issue, as it allows real-time monitoring of the neuronal resting membrane potential during THG image acquisition. By monitoring the resting potential, any effect of the light on the cell would be observed as a deviation from the equilibrium value. Any laser-induced damage to the cell would directly show up as an irreversible change in membrane potential. We perform this experiment by repeatedly recording THG images of a patched cell while monitoring its membrane potential through the patch pipette. This experiment has been repeated at increasing laser intensities, with typical results as shown in Fig. 5*E*. During scanning, only a small increase in membrane potential is observed, which remains fully reversible even at high laser intensity. The fact that the observed membrane potential changes are both reversible and reproducible demonstrates that, while the THG beam does influence the cell slightly, it does not introduce photodamage. It should be stressed here that only part of the 200 mW laser power actually reaches the focus due to scattering by the tissue. Furthermore, a high-contrast image of the cell could already be obtained at significantly lower power in this case (~50 μm depth), so that the change in membrane potential remains at or below the 1%-level for typical imaging conditions.

Fig. 5*F* shows the maximum observed change in resting membrane potential as a function of incident laser power. The observation that the resting membrane potential changes slightly upon illumination indicates that the permeability of the membrane is modified by the light. This effect could have several explanations, which include thermal gradients across the cell or possible (nonlinear) excitation of membrane proteins. It is difficult to conclusively identify the cause of this signal, because the influence of possible molecular excitation on the neuronal membrane potential is unknown. However, the linear dependence on laser intensity seems to indicate that nonlinear effects such as two-photon excitation of endogenous molecules are a less likely cause. It is worth noting that this measurement may well overestimate the influence of the laser light, because also the patch pipette may heat up, causing additional stress on the seal between pipette and cell membrane. A degradation of this seal could easily lead to an increased leak current, which would mimic a change in membrane potential.

Furthermore, we have patched neurons after continuous THG imaging for >5 minutes, and typically observed normal cell behavior and resting membrane potentials, indicating that the cells have not been adversely affected by the incident light. These results clearly show that THG microscopy preserves cell viability even after extended imaging.

In Vivo THG Imaging. To investigate the feasibility of in vivo THG brain imaging, we performed experiments on living, anesthetized mice. A craniotomy provided access to the brain. High-contrast images were obtained, as shown in Fig. S4*A*. The achieved depth range was ~200 micrometers, limited by the laser power and the presence of extended vasculature above the imaging location. An in vivo THG image of blood vessels is shown in Fig. 2*F*. Although the current setup limits the imaging range to layer 2/3 neurons, our in vitro experiments discussed above (see Fig. 4) indicate that a higher pulse intensity could enable a significant improvement in the achievable depth range.

To obtain more information about the origin of the THG signal, transgenic mice expressing GFP in neuronal membranes were used. A high degree of correlation is found between the THG and the GFP images (displayed in Fig. S4 *A* and *B*, respectively). While these experiments do not prove beyond doubt that the observed shadow features are in fact neurons, their shape and size, as well as the THG-GFP correlation provide significant evidence to this end. More importantly, these measurements demonstrate our ability to achieve good contrast and resolution in the brain of a living animal, paving the way for more extensive in vivo studies, as well as various biomedical applications.

Conclusions and Outlook. In conclusion, we demonstrate that optical phase-matching-based contrast mechanisms provide a powerful alternative to fluorescence-based techniques, especially in biomedical applications where the use of dyes may be problematic. By controlling the laser beam parameters, the structure of brain tissue can be used effectively for the generation of intrinsic optical nonlinear contrast, through partial phase matching of THG. THG imaging thus provides a powerful tool for noninvasive optical biopsies of unstained live brain tissue. We anticipate various biomedical applications, such as the use of THG imaging for real-time diagnostic tissue screening during brain surgery, and possibly even for guiding microscopic surgical tools with subcellular precision.

The sensitivity of THG imaging to lipid structures is intriguing, as various diseases in the human brain are accompanied or caused by alterations in lipid metabolism. Abnormal concentrations of lipid droplets have been observed in human brain tumours of various grades (35). Accumulations of cholesterol are found in senile plaques that characterize Alzheimer's disease (36), while various other neurodegenerative disorders are associated with abnormal lipid metabolism (37). The ability to image lipids with intrinsic contrast at cellular resolution may therefore be promising to visualize and study such disorders.

Materials and Methods

THG Imaging. For the THG imaging experiments, we use a commercial two-photon laser-scanning microscope (TrimScope, Lavision BioTec GmbH). The light source is an optical parametric oscillator (Mira-OPO, APE), pumped at 810 nm by a modelocked Ti:Sapphire laser (Coherent Chameleon Ultra II). The light is focused onto the sample using a 20×, 0.95 N.A. water-dipping objective (Olympus XLUMPFL-IR).

The THG experiments described in this paper are performed using an epidetection geometry. The back-scattered THG photons are separated from the incoming laser beam using a dichroic mirror (Chroma T800lpxrxt), and filtered by a band-pass filter at the THG wavelength (Chroma HQ390-70X).

The detector is a GaAsP high-sensitivity photomultiplier tube (Hamamatsu H7422-40), with a quantum efficiency of 25% at 400 nm. Typical image acquisition times are 1.6 s for the highest resolution images (1,024× 1,024 pixels), and 0.6 s for 512 × 512 pixel images, which we used for the targeted patching experiments.

For a comparison with forward-detection, a custom transmission port is used. This port employs a 1.4 N.A. oil immersion condenser, a long-pass

dichroic mirror (UQG optics), and a narrow-band interference filter at 400 nm (Optosigma).

For the combined THG and SR-101 experiments, we use the OPO at 1,200 nm to produce both signals simultaneously. The SR-101 fluorescence is separated from the THG signal using a dichroic mirror with a cutoff at 561 nm and a band-pass filter at 594 nm. The SR-101 signal is detected with a PMT (Hamamatsu H6780-20). Combined Nile Red and THG imaging is also performed by simultaneous excitation using the OPO at 1,200 nm. In this particular case, the THG is measured with the transmission port, while the Nile Red fluorescence is epidetected through a 593/40 nm band-pass filter.

For combined THG and GFP imaging, the Ti:Sapphire laser used to pump the OPO is tuned to 970 nm and coupled into the microscope. The GFP fluorescence and THG signal of a tissue volume are then measured consecutively, using the same detector, but with a different band-pass filter (561/40 nm) for the GFP.

Data acquisition is done with the microscope software (Imspector Pro), and images are stored in 16-bit tiff-format. Images are analyzed using ImageJ (MacBioPhotonics).

Electrophysiology. Whole-cell patch-clamp recordings are taken using an EPC-8 amplifier (HEKA), and digitized with an ITC-8 data acquisition unit. Patch pipettes (3–6 MΩ tip resistance) are drawn from borosilicate glass, fire-polished, and filled with an intracellular solution containing: 120 mM K-gluconate, 10 mM KCl, 10 mM Hepes, 10 mM K-phosphocreatine, 4 mM ATP-Mg, 0.4 mM GTP, and pH adjusted to 7.3 with KOH, final osmolarity 270–285 mOsm. All experiments are performed at room temperature.

All THG-guided label-free targeted patching experiments are performed using an epidetection geometry. We successfully patched >30 cells using this technique, of which seven at a depth >200 μm.

Animal Handling. Brains of C57/BL6 wild-types or Somatostatin-eGFP conjugated GFP-expressing inhibitory neuron line (32) were rapidly removed and dissected in ice-cold artificial cerebrospinal fluid (aCSF) containing the following: 110 mM choline chloride; 11.6 mM sodium ascorbate; 7 mM $MgCl_2$; 3.1 mM Na-pyruvate; 2.5 mM KCl; 1.25 mM NaH_2PO_4; 0.5 mM $CaCl_2$; 26 mM $NaHCO_3$; and 10 mM glucose (~300 mOsm).

Coronal slices of various parts of the brain were cut on a vibrating microtome at 300–350 μm thickness and then placed in a submerged-style holding chamber in aCSF, bubbled with carbogen (95% O_2, 5% CO_2) containing the following: 126 mM NaCl; 3 mM KCl; 1 mM NaH_2PO_4; 1 mM $MgSO_4$; 2 mM $CaCl_2$; 26 mM $NaHCO_3$; and 10 mM glucose. Slices were allowed to recover for 20 min at 33 °C followed by 40 min at room temperature.

For the in vivo experiments, adult EGFP-tKras mice (38) (>5 months old, 30–35 g) are anesthetized using urethane (1.6 g/kg) in 0.9% NaCl. Depth of anaesthesia is checked by both foot and eyelid reflex and vibrissae movements. The animal's temperature is monitored with a rectal probe and maintained at 37 °C by a thermostatically controlled heating pad. Imaging experiments are performed on neocortex relatively free of blood vessels to facilitate THG imaging (usually 10 mm posterior and 1 mm lateral from bregma). A craniotomy of 0.5 by 0.5 mm is made covering the area of interest with the dura removed.

All experimental procedures were carried out according to the animal welfare guidelines of the VU University Amsterdam, the Netherlands.

ACKNOWLEDGMENTS. We acknowledge Dr. R.M. Meredith for experimental assistance, and R. Poorthuis, M. Groen, T. Cijsouw, and Dr. R.F.G. Toonen for providing samples. This work was supported by grants from the Netherlands Organization for Scientific Research (NWO) (917.76.360), Neuroscience Campus Amsterdam, VU University Board (Stg. VU-ERC), and Neurobsik to H.D.M.

1. Tearney GJ, et al. (1997) In vivo endoscopic optical biopsy with optical coherence tomography. *Science* 276:2037–2039.
2. Tsai PS, et al. (2003) All-optical histology using ultrashort laser pulses. *Neuron* 39:27–41.
3. Denk W, Strickler JH, Webb WW (1990) 2-photon laser scanning fluorescence microscopy. *Science* 248:73–76.
4. Helmchen F, Denk W (2005) Deep tissue two-photon microscopy. *Nat Methods* 2:932–940.
5. Dombeck DA, Sacconi L, Blanchard-Desce M, Webb WW (2005) Optical recording of fast neuronal membrane potential transients in acute mammalian brain slices by second-harmonic generation microscopy. *J Neurophysiol* 94:3628–3636.
6. Barad Y, Eisenberg H, Horowitz M, Silberberg Y (1997) Nonlinear scanning laser microscopy by third harmonic generation. *Appl Phys Lett* 70:922–924.
7. Squier JA, Muller M, Brakenhoff GJ, Wilson KR (1998) Third harmonic generation microscopy. *Opt Express* 3:315–324.
8. Yelin D, Silberberg Y (1999) Laser scanning third-harmonic-generation microscopy in biology. *Opt Express* 5:169–175.
9. Debarre D, et al. (2006) Imaging lipid bodies in cells and tissues using third-harmonic generation microscopy. *Nat Methods* 3:47–53.
10. Hsieh CS, et al. (2008) Higher harmonic generation microscopy of in vitro cultured mammal oocytes and embryos. *Opt Express* 16:11574–11588.
11. Evans CL, et al. (2005) Chemical imaging of tissue in vivo with video-rate coherent anti-Stokes Raman scattering microscopy. *Proc Natl Acad Sci USA* 102:16807–16812.
12. Jurna M, et al. (2009) Vibrational phase contrast microscopy by use of coherent anti-Stokes Raman scattering. *Phys Rev Lett* 103:043905.
13. Freudiger CW, et al. (2008) Label-free biomedical imaging with high sensitivity by stimulated Raman scattering microscopy. *Science* 322:1857–1861.
14. Ward JF, New GHC (1969) Optical third harmonic generation in gases by a focused laser beam. *Phys Rev* 185:57–72.
15. Muller M, Squier J, Wilson KR, Brakenhoff GJ (1998) 3D microscopy of transparent objects using third-harmonic generation. *J Microsc* 191:266–274.
16. Lee JH, et al. (2009) Noninvasive in vitro and in vivo assessment of epidermal hyperkeratosis and dermal fibrosis in atopic dermatitis. *J Biomed Opt* 14:014008.
17. Tai SP, et al. (2006) In vivo optical biopsy of hamster oral cavity with epi-third-harmonic-generation microscopy. *Opt Express* 14:6178–6187.
18. Olivier N, et al. (2010) Cell lineage reconstruction of early Zebrafish embryos using label-free nonlinear microscopy. *Science* 329:967–971.
19. Chen SY, et al. (2006) Noninvasive harmonics optical microscopy for long-term observation of embryonic nervous system development in vivo. *J Biomed Opt* 11:054022.
20. Andresen V, et al. (2009) Infrared multiphoton microscopy: subcellular-resolved deep tissue imaging. *Curr Opin Biotechnol* 20:54–62.
21. Debarre D, Supatto W, Beaurepaire E (2005) Structure sensitivity in third-harmonic generation microscopy. *Opt Lett* 30:2134–2136.
22. Barazany D, Basser PJ, Assaf Y (2009) In vivo measurement of axon diameter distribution in the Corpus Callosum of rat brain. *Brain* 132:1210–1220.
23. Cornelisse LN, et al. (2007) High speed two-photon imaging of calcium dynamics in dendritic spines: consequences for spine calcium kinetics and buffer capacity. *PLoS ONE* 2:e1073.
24. Debarre D, Olivier N, Beaurepaire E (2007) Signal epidetection in third-harmonic generation microscopy of turbid media. *Opt Express* 15:8913–8924.
25. Greenspan P, Mayer EP, Fowler SD (1985) Nile Red—a selective fluorescent stain for intracellular lipid droplets. *J Cell Biol* 100:965–973.
26. Dombeck DA, et al. (2003) Uniform polarity microtubule assemblies imaged in native brain tissue by second-harmonic generation microscopy. *Proc Natl Acad Sci USA* 100:7081–7086.
27. Evans CL, et al. (2007) Chemically-selective imaging of brain structures with CARS microscopy. *Opt Express* 15:12076–12087.
28. Kleinfeld D, Mitra PP, Helmchen F, Denk W (1998) Fluctuations and stimulus-induced changes in blood flow observed in individual capillaries in layers 2 through 4 of rat neocortex. *Proc Natl Acad Sci USA* 95:15741–15746.
29. Clay GO, Schaffer CB, Kleinfeld D (2007) Large two-photon absorptivity of hemoglobin in the infrared range of 780–880 nm. *J Chem Phys* 126:025102.
30. Chu SW, et al. (2005) High-resolution simultaneous three-photon fluorescence and third-Harmonic-generation microscopy. *Microsc Res Tech* 66:193–197.
31. Nimmerjahn A, Kirchhoff F, Kerr JND, Helmchen F (2004) Sulforhodamine 101 as a specific marker of astroglia in the neocortex in vivo. *Nat Methods* 1:31–37.
32. Ma YY, et al. (2006) Distinct subtypes of somatostatin-containing neocortical interneurons revealed in transgenic mice. *J Neurosci* 26:5069–5082.
33. Kitamura K, et al. (2008) Targeted patch-clamp recordings and single-cell electroporation of unlabeled neurons in vivo. *Nat Methods* 5:61–67.
34. Komai S, et al. (2006) Two-photon targeted patching (TPTP) in vivo. *Nat Protoc* 1:647–652.
35. Opstad KS, Bel BA, Griffiths JR, Howe FA (2008) An investigation of human brain tumor lipids by high-resolution magic angle spinning H-1 MRS and histological analysis. *NMR Biomed* 21:677–685.
36. Mori T, et al. (2001) Cholesterol accumulates in senile plaques of Alzheimer disease patients and in transgenic APP(sw) mice. *J Neuropathol Exp Neurol* 60:778–785.
37. Liu JP, et al. (2010) Cholesterol involvement in the pathogenesis of neurodegenerative diseases. *Mol Cell Neurosci* 43:33–42.
38. Roelandse M, et al. (2003) Focal motility determines the geometry of dendritic spines. *Neuroscience* 121:39–49.